UC Irvine
UC Irvine Previously Published Works

Title

Evidence for a quantum spin Hall phase in graphene decorated with Bi2Te3 nanoparticles

Permalink
https://escholarship.org/uc/item/62m6t6xj

Journal
Science Advances, 4(11)

ISSN
2375-2548

Authors
Hatsuda, K
Mine, H
Nakamura, T
et al.

Publication Date
2018-11-02

DOI
10.1126/sciadv.aau6915

Copyright Information
This work is made available under the terms of a Creative Commons Attribution License, available at https://creativecommons.org/licenses/by/4.0/

Peer reviewed

eScholarship.org Powered by the California Digital Library
University of California

PHYSICS

Evidence for a quantum spin Hall phase in graphene decorated with Bi_2Te_3 nanoparticles

K. Hatsuda[1], H. Mine[1], T. Nakamura[2], J. Li[3], R. Wu[3], S. Katsumoto[2], J. Haruyama[1,2]*

Copyright © 2018 The Authors, some rights reserved; exclusive licensee American Association for the Advancement of Science. No claim to original U.S. Government Works. Distributed under a Creative Commons Attribution NonCommercial License 4.0 (CC BY-NC).

Realization of the quantum spin Hall effect in graphene devices has remained an outstanding challenge dating back to the inception of the field of topological insulators. Graphene's exceptionally weak spin-orbit coupling—stemming from carbon's low mass—poses the primary obstacle. We experimentally and theoretically study artificially enhanced spin-orbit coupling in graphene via random decoration with dilute Bi_2Te_3 nanoparticles. Multiterminal resistance measurements suggest the presence of helical edge states characteristic of a quantum spin Hall phase; the magnetic field and temperature dependence of the resistance peaks, x-ray photoelectron spectra, scanning tunneling spectroscopy, and first-principles calculations further support this scenario. These observations highlight a pathway to spintronics and quantum information applications in graphene-based quantum spin Hall platforms.

INTRODUCTION

Graphene played a key historical role in the development of topological insulators (*1*, *2*)—materials that exhibit an electrically inert interior yet form exotic metals at their boundary. In 2005, Kane and Mele (*3*) predicted that coupling between the spin and orbital motion of electrons turns graphene into a "quantum spin Hall (QSH)" insulator that hosts spin-filtered metallic edge states with inherent resilience from scattering. These novel edge states underlie tantalizing technological applications for low-power electronics, spintronic devices, and fault-tolerant quantum computing (*4*–*6*). Although graphene's intrinsic spin-orbit coupling is far too weak to produce an observable QSH phase in practice, numerous alternative platforms were subsequently discovered, including HgTe (*7*–*10*) and InAs/GaSb quantum wells (*11*, *12*), WTe_2 (*13*–*15*), bismuthene (*16*), and the layered compound $Bi_{14}Rh_3I_9$ (*17*, *18*).

Ease of fabrication, measurement, and manipulation of graphene nevertheless continues to strongly motivate efforts at fulfilling Kane and Mele's original vision. Might it be possible to externally boost graphene's spin-orbit coupling to stabilize a robust QSH phase, in turn opening an appealing pathway toward applications? Numerous theories have pursued this line of attack via introduction of foreign atoms or via substrate engineering (*19*–*22*); these methods have been predicted to elevate the bulk bandgap for the QSH phase by several orders of magnitude compared to that in pure graphene. Implementation of these proposals has, however, so far proven challenging despite recent efforts (*23*–*26*).

Here, we present the first experimental evidence for the formation of an "engineered" QSH phase in a graphene device. Specifically, we explore graphene decorated with dilute, randomly positioned Bi_2Te_3 nanoparticles. These nanoparticles carry giant spin-orbit coupling via tunneling current and can thus significantly modify graphene's electronic structure even at very low coverages (*26*); they can also be inserted into the graphene lattice in a minimally invasive manner. As theoretically demonstrated on heavy adatom/graphene systems (e.g., Os atom) in our previous study (*20*), topological bulk gaps open due to the hybridization between the graphene's π states (Dirac state) and the spin-orbit split d_{xz} and d_{yz} Os-atom orbitals in the case of Os adatom. The Dirac state of graphene is rather delocalized, and thus, it can highly mediate interactions among Os adatoms over a large range even under small coverages. Qualitatively similar results are expected in the present system with small coverage ratios of heavy nanoparticles. We perform nonlocal resistance measurements on multiple devices and find quantitative agreement with the response expected from dissipationless edge-state conduction in a QSH phase. The perpendicular magnetic field and temperature dependence of the observed resistance peaks, scanning tunneling spectroscopy (STS), and first-principles simulations further corroborate this picture. Our results reestablish graphene as an experimentally promising QSH medium and spotlight many avenues of future exploration.

RESULTS

In the present experiments, monolayer graphene is grown by chemical vapor deposition (CVD) on a SiO_2/Si substrate (area, ~1 cm^2) and formed into Hall bar patterns by argon gas etching with six or four branches to Ti/Au electrode terminals (see Fig. 1, A to D, and fig. S1). Similar multiterminal devices have been used to detect helical edge states in HgTe quantum wells (*8*). The high quality of the monolayer graphene (i.e., low amounts of defects and contamination) is confirmed by Raman spectroscopy and x-ray photoelectron spectroscopy (XPS).

We further deposit Bi_2Te_3 nanoparticles with diameters of ~1 to 30 nm (Sigma-Aldrich Inc.) onto the graphene surface following our previous nanoneedle method [section S2 and (*26*)]. Specifically, for the present experiment, we repeatedly drop and then absorb a small acetone droplet containing the nanoparticles using the narrow tip of the needle (Saito Medical Instruments Inc.), which has an inner pore diameter of ~50 μm, allowing precise control of the low nanoparticle density D within the small graphene Hall bar (section S2 and movie S1). Figure 1E shows an AFM image of a decorated sample with mean $D \sim 4/100^2$ nm^2 (~3% coverage ratio for the particles with a diameter of ~10 nm), which we used for the present experiments. This coverage ratio may become somewhat higher when subnanoparticles formed by ultrasonication exist (section S2), although they cannot be confirmed in Fig. 1E. XPS spectra of the samples after the

[1]Faculty of Science and Engineering, Aoyama Gakuin University, 5-10-1 Fuchinobe, Sagamihara, Kanagawa 252-5258, Japan. [2]Institute for Solid State Physics, The University of Tokyo, 5-1-5 Kashiwanoha, Kashiwa, Chiba 277-8581, Japan. [3]Department of Physics and Astronomy, University of California, Irvine, Irvine, CA 92697-4575, USA.
*Corresponding author. Email: j-haru@ee.aoyama.ac.jp

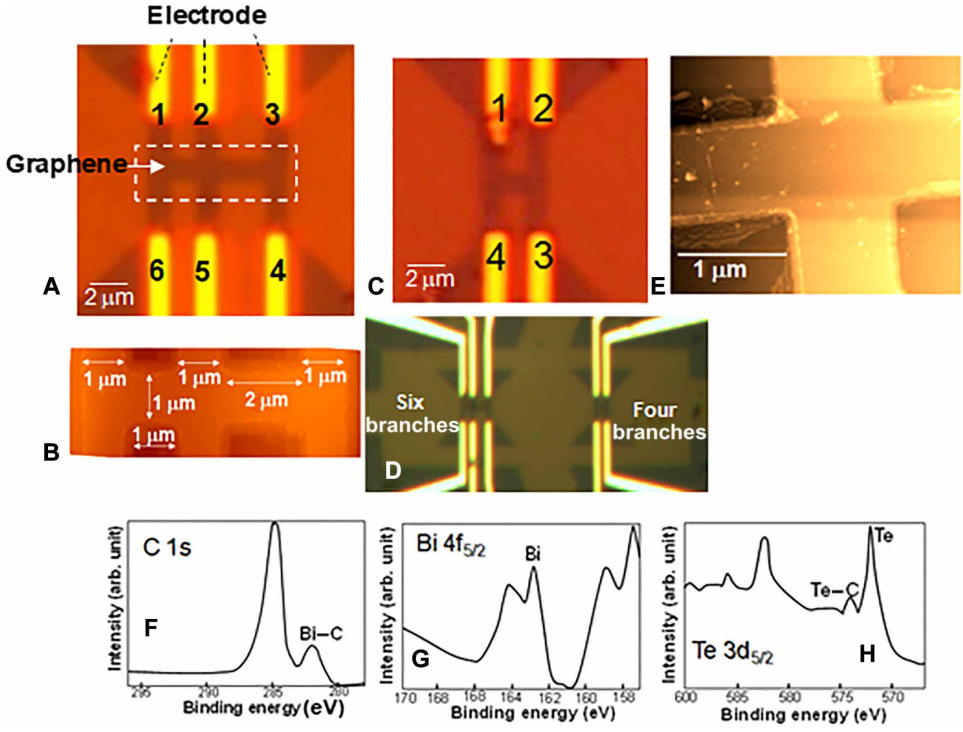

Fig. 1. Sample fabrication and characterization. (**A** to **C**) Atomic force microscopy (AFM) images of graphene Hall bar devices used for resistance measurements of Fig. 2. (B) Expansion of the dashed rectangle in (A). For (C), the channel and branch widths are ~1 μm. (**D**) Optical microscopy image of devices in (A) and (C), which are formed at neighboring position on the same segment of CVD-grown graphene (section S1). (**E**) AFM image of graphene decorated with Bi_2Te_3 nanoparticles at $D \sim 4/100^2$ nm^2 (~3% coverage ratio); the image is taken at the center of the six branches of (A). (**F** to **H**) XPS spectra of the samples.

annealing at 400°C (section S2) (Fig. 1, F to H) demonstrate a C 1s orbital peak (~282 eV) arising from Bi–C coupling (Fig. 1F) and a Te $3d_{5/2}$ orbital peak (~574 eV) arising from Te–C coupling (Fig. 1H). These peaks suggest clean, low-damage decoration with Bi_2Te_3 nanoparticles and also indicate the hybridization required for enhancing graphene's spin-orbit coupling as mentioned above.

Figure 2 shows four-probe resistance measurements obtained in the six- and four-terminal (branch) devices from Fig. 1 (A and C). Current I_{ij} flows from lead i to lead j, and the voltage V_{kl} is measured across contacts k and l, yielding a resistance $R_{ij,kl} = V_{kl}/I_{ij}$ that we monitor as a function of back-gate voltage V_{bg}. In a QSH phase, conduction is mediated by helical edge states that equilibrate at the contacts but are otherwise protected from elastic backscattering by time-reversal symmetry. Landauer-Buttiker formalism (*9*) then predicts $R_{ij,kl}$ values quantized to rational fractions of the resistance quantum $R_Q = h/e^2$, where h is Planck's constant and e is the electron charge. Quantized nonlocal resistances have been previously reported in HgTe quantum wells as evidence for dissipationless helical edge transport (*9*). Figure 2A illustrates $R_{16,34}$ measured for undecorated graphene and with Bi_2Te_3 nanoparticles at a coverage of ~3%. As expected, without nanoparticles, $R_{16,34}$ (measured at room temperature) essentially vanishes for all V_{bg}. Nanoparticle decoration, by contrast, yields an appreciable nonlocal resistance $R_{16,34}$ even at room temperature. Upon cooling down to $T = 1.5$ K, we find an extended V_{bg} window for which a maximum of $R_{16,34} \approx R_Q/6$ appears—in quantitative agreement with the value expected from helical edge transport.

All other panels in Fig. 2 correspond to measurements on Bi_2Te_3-decorated graphene at $T = 1.5$ K. Figure 2B plots $R_{13,46}$, which peaks at ~$2R_Q/3$, while Fig. 2C shows $R_{14,23}$, which peaks at ~$R_Q/2$. (The pronounced minimum in $R_{14,23}$ at V_{bg} ~10 V possibly arises from a leakage current between the electrode pad 1 and back-gate electrode through the p-type silicon substrate.) Figure 2D shows $R_{14,23}$ for a four-terminal H-shaped device at a coverage of ~3%; this nonlocal resistance peaks at ~$R_Q/4$. The peak values in Fig. 2 (B to D) also agree quantitatively with the helical edge-state picture. Four samples among the fabricated 10 samples have demonstrated these R peaks to date. However, the observed $R_{45,13}$ from our six-terminal device (Fig. 2E) significantly overshoots the resistance $R_Q/3$ expected from helical edge states. The origin of this discrepancy is presently unclear. We also detected nonlocal resistances in four other devices that significantly undershoot the predicted quantized values—possibly indicating shorting of the current through the bulk of these samples.

Figure 3A illustrates examples of STS measurements on the decorated graphene devices. No energy gaps are observed with V_{bg}, away from the resistance peaks in Fig. 2. Adjusting V_{bg} (e.g., 24 V) to those coincident with resistance peaks in Fig. 2 yields qualitatively different behavior. For two spectra taken near two different nanoparticles existing at bulk, clear spectral gaps are visible, ranging in magnitude from ~5 to 20 meV. This variation is consistent with simulations, as explained later (Fig. 4 and section S3), which reveal nonuniformity of these gaps as arising from variations in the nanoparticle size, chemical condition (e.g., stoichiometry), and their chemical bonding with graphene Dirac states. By contrast, data taken at an edge point show disappearance of these gaps. Note that these "V-shaped"–like edge spectra qualitatively resemble STS measurements in several other QSH candidates (*14*, *16*, *18*). Collectively, our STS experiments further support the emergence of an insulating bulk with gapless helical edge states driven by nanoparticle decoration.

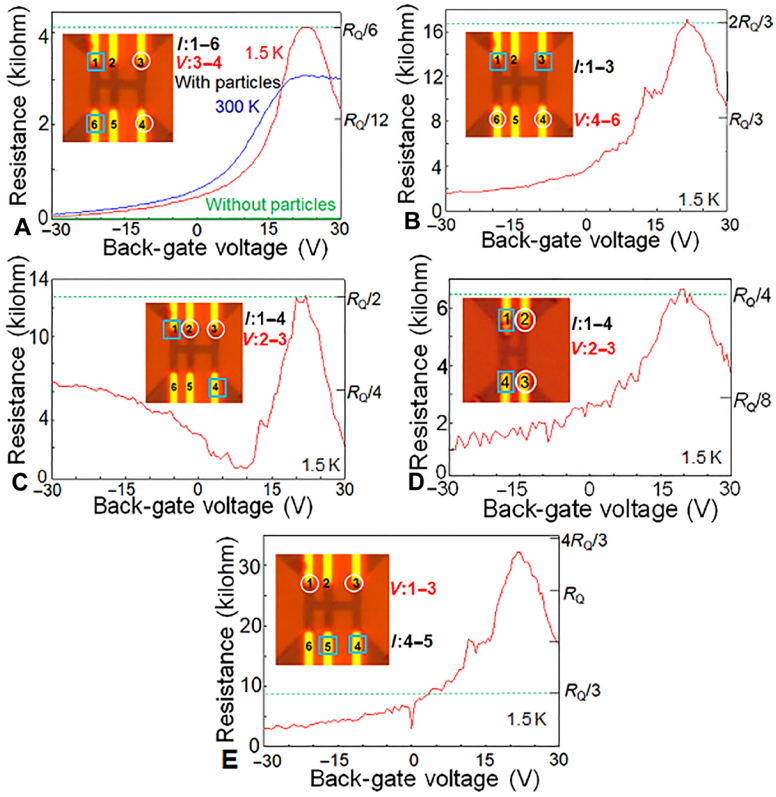

Fig. 2. Four-probe resistances versus back-gate voltage (V_{bg}) measured on the samples shown in Fig. 1. (**A** to **E**) Current flows between contacts indicated by squares, and voltage is measured across circled contacts; no contact resistances are subtracted. In (A), the green line corresponds to undecorated graphene. All other data correspond to graphene with nanoparticles at a coverage ratio of ~3%. The green dashed line in each panel represents quantized resistances predicted for helical edge transport (R_Q is the resistance quantum).

Figure 3B shows the out-of-plane magnetic field ($B_\perp$) dependence of the conductance (G), corresponding to the inverse of the R peak values of Fig. 2 (A, blue symbol, and D, red symbol) and the two off–R peak values (green and pink symbols). The two G values for the two R peaks exponentially decrease with increasing $B_\perp$, whereas G for the off–R peak values decreases just slightly. These behaviors qualitatively agree with a QSH phase observed in monolayer WTe_2 (*15*) and support the attribution of the two R peaks of Fig. 2 (A and D) to the helical edge spins. A QSH phase emerges with a bulk energy gap but gapless helical edge states protected by time-reversal symmetry, in which opposite spin states form a Kramers doublet and counter-propagate. Only when a Fermi level is set to the Kramers point, R values (G values in Fig. 3B) can sufficiently reflect the bandgap opening at the edges due to the Zeeman effect caused by applying $B_\perp$, resulting in the observed decrease in G corresponding to the two R peaks.

Almost the same slope values of the linear decreases in two G, for the six- and four-probe patterns, suggest that dephasing in metal electrodes is not much influenced by applying $B_\perp$ and only resolving in degeneracy in the Kramers doublet due to the Zeeman effect is caused over all the sample edges. This proves that the helical edge mode paths continuously exist along the sample edge, despite the presence of the multiple metal electrodes. The applied $B_\perp$ has almost no influence on the magnetization of Bi_2Te_3 nanoparticles, because almost no magnetization is observed in the magnetization curve (i.e., the amplitude of the diamagnetism observed around $B = 0$ is as small as ~10^{-7} emu and the magnetism observed at high B is smaller than ~10^{-6} emu) even for graphene decorated with Bi_2Te_3 nanoparticles at a coverage as large as ~10% on application of $B_\perp$ (Fig. 3C and section S2). The coverages of the samples used for the R measurements are much smaller (<3%), and hence, magnetization is almost absent.

Figure 3D shows the zero-B temperature dependence of G (in Alenius plot format) corresponding to the inverse of the R peak values of Fig. 2 (A, blue symbol, and D, red symbol). The G values are constant at low temperatures, while they linearly increase above T_c = 20 and 25 K for the blue and red symbols, respectively, as temperature increases, following thermal activation relationships. The slope values of the linear increases in two G are slightly different with activation energies of ~20 and ~25 meV for the blue and red symbols, respectively, which approximately agree with the bulk gap values observed in the STS. Three possible origins are considered for these deviations from $(R_Q/6)^{-1}$ and $(R_Q/4)^{-1}$ at high temperatures: (i) the contribution of thermally activated carriers over the bulk gap, (ii) spin fluctuation in helical edge spins, and (iii) induced dephasing in metal electrodes. The agreement with the STS observation suggests that (i) is the dominant factor. Because the activation energy observed at $B = 0$ correspond to the bulk gap, this is consistent. Slightly lower T_c (=20 K) in the six-probe sample compared with T_c (=25 K) in the four-probe sample is also attributed to the smaller bulk gap.

DISCUSSION

To explain these experimental findings, we performed density functional theory (DFT) calculations using a large 7 × 7 graphene supercell

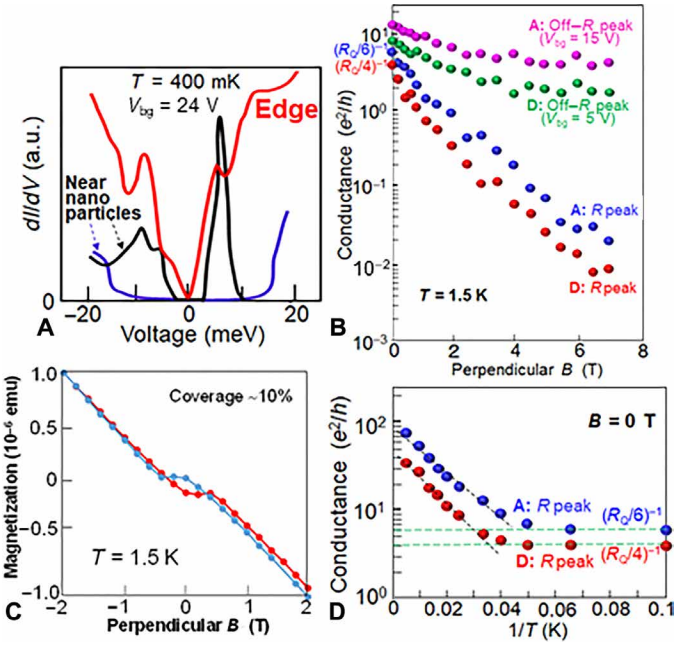

Fig. 3. Reconfirmation of QSH phase. (**A**) STS spectra for a sample around V_{bg} for *R* peak, recorded at bulk locations near two different nanoparticles (~50 to 80 nm from particles), showing the maximum (~20 meV; blue line) and minimum (~5 meV; black line) gaps, and at an edge point (~50 nm from edges and ~200 nm away from nanoparticles), revealing the gap disappearance (red line). a.u., arbitrary units. (**B**) Perpendicular magnetic field ($B_\perp$) dependence of conductance (*G*) corresponding to the inverse of the *R* peak values of Fig. 2 (A, blue symbol, and D, red symbol) and two off–*R* peak values (pink and green symbols in Fig. 2, A and D, respectively). (**C**) Magnetization curve for graphene decorated with Bi_2Te_3 nanoparticles at a coverage as large as ~10%, on application of $B_\perp$. (**D**) Zero-*B* temperature dependence of conductance (in Alenius plot format) corresponding to the inverse of the *R* peak values shown in Fig. 2 (A, blue symbol, and D, red symbol); the dashed lines serve as a guide to the eye.

containing a Bi_2Te_3 nanoparticle with 10 Bi and 15 Te atoms (the diameter of this cluster is about 1.2 nm). Because the atomic structure of the nanoparticle is unknown, we performed ab initio molecular dynamics (AIMD) simulations by baking it at 600 K for 6 ps and then cooling it down to 300 K in 5 ps. The structures obtained through AIMD simulations were further relaxed at 0 K, with the inclusion of the van der Waals correction in DFT calculations. Figure 4 (A and B) shows side and top views of the optimized structure of the Bi_2Te_3 nanoparticle on graphene. The separation between the nanoparticle and graphene is about 3.4 Å, indicating weak interaction between them—contrary to single Bi atoms, which hybridize strongly with graphene. Moreover, a small corrugation appears in the graphene layer. From the charge-density difference ($\Delta\rho = \rho_{BT/Gr} - \rho_{BT} - \rho_{Gr}$), we see that Bi atoms donate electrons to graphene, whereas Te atoms gain electrons from graphene.

Because of the weak van der Waals interaction, the composite system's band structure continues to exhibit Dirac cones (Fig. 4C). Electronic states of the Bi_2Te_3 nanoparticle reside rather far from the Fermi level and disperse weakly, indicating adequacy of the 7 × 7 supercell for minimizing direct interaction among adjacent nanoparticles. Significantly, Bi_2Te_3 nanoparticles nevertheless yield a sizeable bandgap $E_g \approx 6$ meV at the Dirac point, which sits slightly away from the Fermi level due to the aforementioned charge transfer (Fig. 4D). To determine whether the bandgap is topologically non-

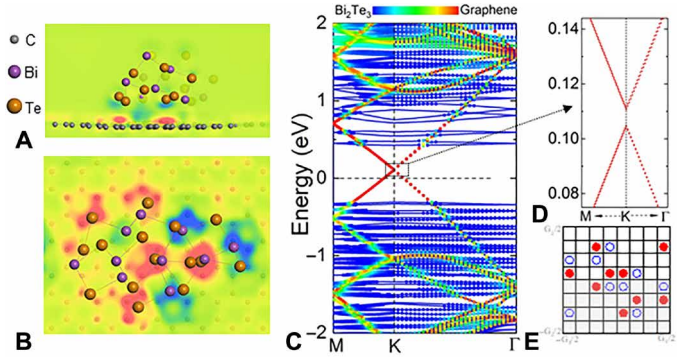

Fig. 4. Theoretical calculations. (**A** and **B**) Side and top views of the atomic structure and charge-density difference of Bi_2Te_3/graphene. Red and blue colors indicate charge depletion and accumulation, respectively. (**C** and **D**) Band structure of Bi_2Te_3/graphene. (**E**) *n*-field configuration with red solid, blue hollow circles, and blank boxes denoting $n = -1$, 1, and 0, respectively. Summing the *n*-fields over half of the torus yields a nontrivial Z_2 invariant.

trivial, we calculated the *n*-fields and Z_2 invariant from the Bloch functions (Fig. 4E) (*27*, *28*). By counting the positive and negative *n*-field numbers over the half of the torus (see Fig. 4E), one obtains a nontrivial Z_2 invariant. Test calculations with different *k*-point meshes consistently reproduce this result. Therefore, DFT predicts that Bi_2Te_3 nanoparticle–decorated graphene realizes a QSH phase, supporting our experimental observations.

To establish robustness of the topological state, we calculated the band structures and Z_2 invariants using an 8 × 8 supercell with Bi_2Te_3 nanoparticles containing an additional Bi or Te atom. The altered chemical stoichiometry of the nanoparticles shifts the Fermi level, as shown in fig. S3 (section S3). Furthermore, the reduction of Bi_2Te_3 coverage in the 8 × 8 supercell produces a bandgap that is reduced (fig. S2) yet remains topologically nontrivial in both cases. The bandgap magnitude and Fermi-level position thus appear to be tunable by adjusting the size, coverage, and stoichiometry of Bi_2Te_3 nanoparticles. These features are consistent with STS observations, which demonstrated nonuniform gaps depending on nanoparticles (Fig. 2F), and are attractive for the development of graphene-based QSH devices.

CONCLUSION

In conclusion, multiterminal *R* measurements, those $B_\perp$ and temperature dependence, XPS, STS, and first-principles calculations provided strong evidence that helical edge states characteristic of a QSH phase emerge upon random decoration of dilute Bi_2Te_3 nanoparticles (as small as ~3%) into graphene via our nanoneedle method. On the contrary, edge states can arise even in topologically trivial systems (*29*–*31*), e.g., due to band bending (*30*) and edge defects (*31*) as observed recently in ordinary graphene near the Dirac point. Although quantized edge resistances were not reported in those graphene studies, it may be important to ask whether our experiments are compatible with such a trivial scenario. Systematically exploring the effects of nanoparticle positions, sizes, and stoichiometry would help further clarify the present QSH phase. It is highly expected that these experiments will introduce robust QSH phase to the present graphene and open the doors to innovative spintronic devices and quantum information applications in graphene-based QSH platforms.

MATERIALS AND METHODS

Formation of graphene to small Hall bar patterns with branches

CVD-grown monolayer graphene with 1-cm^2 area was formed into nine segments (see section S1 and fig. S1A), including the two Hall bar patterns with six or four branches in individual segments, by Ar gas etching (Fig. 1D; fig. S1, B and C; and section S1).

Nanoneedle decoration of Bi_2Te_3 nanoparticles

Before Bi_2Te_3 nanoparticle decoration, an acetone solution containing the nanoparticles (Sigma-Aldrich Inc.) was ultrasonicated for 3 to 5 hours by low power to obtain much smaller particle diameters (e.g., <1 nm) by crushing them, avoiding introduction of defects to nanoparticles. Then, a low amount of acetone solution containing Bi_2Te_3 nanoparticles (e.g., 0.01 mg/8 ml) was dropped from the top end of the nanoneedle (Saito Medical Instruments Inc.) on the two neighboring Hall bar patterns of graphene (section S1 and fig. S1C). This droplet on graphene was then absorbed by the nanoneedle (see movie S1). We repeated this dropping and absorbing 10 to 20 times, resulting in the controlled decoration of Bi_2Te_3 nanoparticles with very low density (<5% coverage).

The obtained density and distribution of nanoparticles on the patterned graphene was sensitive to the density of nanoparticles contained in acetone solution, time for ultrasonication of the solution, position to absorb the solution by a nanoneedle from a container right after the ultrasonication, and the number of times to repeat the dropping and absorbing as mentioned above. Because the deposited nanoparticles were spread over a large area of the sample (e.g., over the region for section S1 and fig. S1B) depending on this optimized condition, a passivation film with an open window only on the graphene surface (e.g., section S1 and fig. S1C) was needed. After the decoration, each sample was annealed at 400°C for 10 to 15 min under a high vacuum (10^{-6} torr) for surface cleaning. These annealing conditions were the upper limit to keep the quality of the nanoparticles. Nanoparticles annealed at 450°C with the same time and vacuum degraded.

SUPPLEMENTARY MATERIALS

Supplementary material for this article is available at http://advances.sciencemag.org/cgi/content/full/4/11/eaau6915/DC1

Section S1. Formation of graphene to small Hall bar patterns with branches

Section S2. Nanoneedle decoration of Bi_2Te_3 nanoparticles

Section S3. DFT calculation methods

Fig. S1. Designs of graphene Hall bars.

Fig. S2. DFT calculation results for $Bi_{10}Te_{15}$/graphene using an 8×8 supercell.

Fig. S3. Same as fig. S2, but for $Bi_{11}Te_{15}$/graphene in a 7×7 supercell.

Fig. S4. Spatial distributions of states at the tips of the Dirac cones for $Bi_{10}Te_{15}$/graphene in a 7×7 supercell.

Movie S1. How to decorate Bi_2Te_3 nanoparticles with very low amount by a nanoneedle

References (*32*–*38*)

REFERENCES AND NOTES

1. M. Z. Hasan, C. L. Kane, *Colloquium*: Topological insulators. *Rev. Mod. Phys.* **82**, 3045–3067 (2010).
2. X.-L. Qi, S.-C. Zhang, Topological insulators and superconductors. *Rev. Mod. Phys.* **83**, 1057–1110 (2011).
3. C. L. Kane, E. J. Mele, Quantum spin Hall effect in graphene. *Phys. Rev. Lett.* **95**, 226801 (2005).
4. L. Fu, C. L. Kane, Josephson current and noise at a superconductor-quantum spin Hall insulator-superconductor junction. *Phys. Rev. B* **79**, 161408 (2009).
5. A. Yu. Kitaev, Fault-tolerant quantum computation by anyons. *Ann. Phys.* **303**, 2–30 (2003).
6. C. Nayak, S. H. Simon, A. Stern, M. Freedman, S. D. Sarma, Non-Abelian anyons and topological quantum computation. *Rev. Mod. Phys.* **80**, 1083–1159 (2008).
7. B. A. Bernevig, T. L. Hughes, S.-C. Zhang, Quantum spin Hall effect and topological phase transition in HgTe quantum wells. *Science* **314**, 1757–1761 (2006).
8. M. König, S. Wiedmann, C. Brüne, A. Roth, H. Buhmann, L. W. Molenkamp, X.-L. Qi, S.-C. Zhang, Quantum spin Hall insulator state in HgTe quantum wells. *Science* **318**, 766–770 (2007).
9. A. Roth, C. Brüne, H. Buhmann, L. W. Molenkamp, J. Maciejko, X.-L. Qi, S.-C. Zhang, Nonlocal transport in the quantum spin Hall state. *Science* **325**, 294–297 (2009).
10. C. Brüne, A. Roth, H. Buhmann, E. M. Hankiewicz, L. W. Molenkamp, J. Maciejko, X.-L. Qi, S.-C. Zhang, Spin polarization of the quantum spin Hall edge states. *Nat. Phys.* **8**, 485–490 (2012).
11. L. Du, I. Knez, G. Sullivan, R.-R. Du, Robust helical edge transport in gated InAs/GaSb bilayers. *Phys. Rev. Lett.* **114**, 096802 (2015).
12. C. Liu, T. L. Hughes, X.-L. Qi, K. Wang, S.-C. Zhang, Quantum spin Hall effect in inverted type-II semiconductors. *Phys. Rev. Lett.* **100**, 236601 (2008).
13. X. Qian, J. Liu, L. Fu, J. Li, Quantum spin Hall effect in two-dimensional transition metal dichalcogenides. *Science* **346**, 1344–1347 (2014).
14. S. Tan, C. Zhang, D. Wong, Z. Pedramrazi, H.-Z. Tsai, C. Jia, B. Moritz, M. Claassen, H. Ryu, S. Kahn, J. Jiang, H. Yan, M. Hashimoto, D. Lu, R. G. Moore, C.-C. Hwang, C. Hwang, Z. Hussain, Y. Chen, M. M. Ugeda, Z. Liu, X. Xie, T. P. Devereaux, M. F. Crommie, S.-K. Mo, Z.-X. Shen, Quantum spin Hall state in monolayer 1T′-WTe_2. *Nat. Phys.* **13**, 683–687 (2017).
15. S. Wu, V. Fatemi, Q. D. Gibson, K. Watanabe, T. Taniguchi, R. J. Cava, P. Jarillo-Herrero, Observation of the quantum spin Hall effect up to 100 kelvin in a monolayer crystal. *Science* **359**, 76–79 (2018).
16. F. Reis, G. Li, L. Dudy, M. Bauernfeind, S. Glass, W. Hanke, R. Thomale, J. Schäfer, R. Claessen, Bismuthene on a SiC substrate: A candidate for a high-temperature quantum spin Hall material. *Science* **357**, 287–290 (2017).
17. B. Rasche, A. Isaeva, M. Ruck, S. Borisenko, V. Zabolotnyy, B. Büchner, K. Koepernik, C. Ortix, M. Richter, J. van den Brink, Stacked topological insulator built from bismuth-based graphene sheet analogues. *Nat. Mater.* **12**, 422–425 (2013).
18. C. Pauly, B. Rasche, K. Koepernik, M. Liebmann, M. Pratzer, M. Richter, J. Kellner, M. Eschbach, B. Kaufmann, L. Plucinski, C. M. Schneider, M. Ruck, J. van den Brink, M. Morgenstern, Subnanometre-wide electron channels protected by topology. *Nat. Phys.* **11**, 338–343 (2015).
19. C. Weeks, J. Hu, J. Alicea, M. Franz, R. Wu, Engineering a robust quantum spin Hall state in graphene via adatom deposition. *Phys. Rev. X* **1**, 021001 (2011).
20. J. Hu, J. Alicea, R. Wu, M. Franz, Giant topological insulator gap in graphene with 5d adatoms. *Phys. Rev. Lett.* **109**, 266801 (2012).
21. H. Jiang Z. Qiao, H. Liu, J. Shi, Q. Niu, Stabilizing topological phases in graphene via random adsorption. *Phys. Rev. Lett.* **109**, 116803 (2012).
22. Y. Ren, Z. Qiao, Q. Niu, Topological phases in two-dimensional materials: A review. *Rep. Prog. Phys.* **79**, 066501 (2016).
23. Z. Jia, B. Yan, J. Niu, Q. Han, R. Zhu, D. Yu, X. Wu, Transport study of graphene adsorbed with indium adatoms. *Phys. Rev. B* **91**, 085411 (2015).
24. U. Chandni, E. A. Henriksen, J. P. Eisenstein, Transport in indium-decorated graphene. *Phys. Rev. B* **91**, 245402 (2015).
25. Y. Wang, S. Xiao, X. Cai, W. Bao, J. Reutt-Robey, M. S. Fuhrer, Electronic transport properties of Ir-decorated graphene. *Sci. Rep.* **5**, 15764 (2015).
26. T. Nanba, K. Tamura, K. Hatsuda, T. Nakamura, C. Ohata, S. Katsumoto, J. Haruyama, Spin–orbit interaction in Pt or Bi_2Te_3 nanoparticle-decorated graphene realized by a nanoneedle method. *Appl. Phys. Lett.* **113**, 053106 (2018).
27. T. Fukui, Y. Hatsugai, Quantum spin Hall effect in three dimensional materials: Lattice computation of Z_2 topological invariants and its application to Bi and Sb. *J. Phys. Soc. Jpn.* **76**, 053702 (2007).
28. D. Xiao, Y. Yao, W. Feng, J. Wen, W. Zhu, X.-Q. Chen, G. M. Stocks, Z. Zhang, Half-Heusler compounds as a new class of three-dimensional topological insulators. *Phys. Rev. Lett.* **105**, 096404 (2010).
29. F. Nichele, H. J. Suominen, M. Kjaergaard, C. M. Marcus, E. Sajadi, J. A. Folk, F. Qu, A. J. A. Beukman, F. K. de Vries, J. van Veen, Edge transport in the trivial phase of InAs/GaSb. *New J. Phys.* **18**, 083005 (2016).
30. M. T. Allen, O. Shtanko, I. C. Fulga, A. R. Akhmerov, K. Watanabe, T. Taniguchi, P. Jarillo-Herrero, L. S. Levitov, A. Yacoby, Spatially resolved edge currents and guided-wave electronic states in graphene. *Nat. Phys.* **12**, 128–133 (2016).
31. M. J. Zhu, A. V. Kretinin, M. D. Thompson, D. A. Bandurin, S. Hu, G. L. Yu, J. Birkbeck, A. Mishchenko, I. J. Vera-Marun, K. Watanabe, T. Taniguchi, M. Polini, J. R. Prance, K. S. Novoselov, A. K. Geim, M. Ben Shalom, Edge currents shunt the insulating bulk in gapped graphene. *Nat. Commun.* **8**, 14552 (2017).
32. G. Kresse, J. Furthmüller, Efficiency of ab-initio total energy calculations for metals and semiconductors using a plane-wave basis set. *Comput. Mater. Sci.* **6**, 15–50 (1996).
33. G. Kresse, J. Furthmüller, Efficient iterative schemes for *ab initio* total-energy calculations using a plane-wave basis set. *Phys. Rev. B* **54**, 11169–11186 (1996).

34. J. P. Perdew, K. Burke, M. Ernzerhof, Generalized gradient approximation made simple. *Phys. Rev. Lett.* **77**, 3865–3868 (1996).
35. P. E. Blöchl, Projector augmented-wave method. *Phys. Rev. B* **50**, 17953–17979 (1994).
36. G. Kresse, D. Joubert, From ultrasoft pseudopotentials to the projector augmented-wave method. *Phys. Rev. B* **59**, 1758–1775 (1999).
37. P. Sony, P. Puschnig, D. Nabok, C. Ambrosch-Draxl, Importance of van der Waals interaction for organic molecule-metal junctions: Adsorption of thiophene on Cu(110) as a prototype. *Phys. Rev. Lett.* **99**, 176401 (2007).
38. J. Klimeš, D. R. Bowler, A. Michaelides, Van der Waals density functionals applied to solids. *Phys. Rev. B* **83**, 195131 (2011).

Acknowledgments: J.H. thanks J. Alicea, Y. Shimazaki, T. Yamamoto, S. Tarucha, T. Ando, S. Tang, Z.-X. Shen, M. Dresselhaus, J. Shi, P. Jarillo-Herrero, A. H. Macdonald, and P. Kim for their technical contributions, fruitful discussions, and encouragement. **Funding:** The work at the Aoyama Gakuin University was partly supported by a grant for private universities and a Grant-in-Aid for Scientific Research (15K13277) awarded by MEXT. Work at the University of Tokyo was partly supported by Grant-in-Aid for Scientific Research (grant no. 26103003). DFT calculations at UCI were supported by DOE-BES (grant no. DE-FG02-05ER46237), and the computer simulations were supported by the National Energy Research Scientific Computing Center (NERSC). **Author contributions:** J.H., S.K., and R.W. conceived the ideas. K.H., H.M., and T.N. carried out the experiments and measurements. J.L. and R.W. performed the calculations. J.H. and R.W. wrote the manuscript. **Competing interests:** The authors declare that they have no competing interests. **Data and materials availability:** All data needed to evaluate the conclusions in the paper are present in the paper and/or the Supplementary Materials. Additional data related to this paper may be requested from the authors.

Submitted 6 July 2018
Accepted 10 October 2018
Published 9 November 2018
10.1126/sciadv.aau6915

Citation: K. Hatsuda, H. Mine, T. Nakamura, J. Li, R. Wu, S. Katsumoto, J. Haruyama, Evidence for a quantum spin Hall phase in graphene decorated with Bi_2Te_3 nanoparticles. *Sci. Adv.* **4**, eaau6915 (2018).